Chinese Chemical Letters 34 (2023) 108283

Contents lists available at ScienceDirect

Chinese Chemical Letters

journal homepage: www.elsevier.com/locate/cclet

High mass-loading α-Fe_2O_3 nanoparticles anchored on nitrogen-doped wood carbon for high-energy-density supercapacitor

Gaigai Duan[a], Hua Zhang[b,*], Chunmei Zhang[c,*], Shaohua Jiang[a,*], Haoqing Hou[b]

[a] *Jiangsu Co-Innovation Center of Efficient Processing and Utilization of Forest Resources, College of Materials Science and Engineering, Nanjing Forestry University, Nanjing 210037, China*
[b] *College of Chemistry and Chemical Engineering, Jiangxi Normal University, Nanchang 330022, China*
[c] *Institute of Materials Science and Devices, School of Materials Science and Engineering, Suzhou University of Science and Technology, Suzhou 215009, China*

ARTICLE INFO

Article history:
Received 20 January 2023
Revised 15 February 2023
Accepted 1 March 2023
Available online 4 March 2023

Keywords:
α-Fe_2O_3 nanoparticles
High mass-loading
Synergistic effect
Interfacial interaction
Energy density

ABSTRACT

The trade-off between mass-loading and cycling stability is always a big challenge for iron oxide-based electrodes. Herein, α-Fe_2O_3 nanoparticles uniformly anchored on nitrogen-doped wood carbons with high mass-loading have been synthesized *via* a facile electrodeposition method accompanied by post-heating treatment. The resultant composite delivers a high specific capacitance of 603 F/g at 0.1 A/g and superior capacitance retention of 85.5% after 10,000 cycles at 10 A/g, indicating excellent long-term cycling stability. Such excellent electrochemical performance can be attributed to the synergistic effects of α-Fe_2O_3 nanoparticles and the conductive matrix as well as the formation of interfacial Fe-O-C bonding, which enables the composite electrode to provide plenty of accessible redox active sites, sufficient electron transport and electrolyte ions diffusion, and robust interfacial interaction. Consequently, the asymmetrical supercapacitor exhibits a high energy density of 30.3 Wh/kg at 125 W/kg, suggesting its great potential for practical applications.

Supercapacitors have been recognized as promising and high-efficiency power sources for electric vehicles, portable electronics, and renewable energy systems owing to their desirable characteristics of high-power density, superior rate capability, and long cycle stability [1–7]. Unfortunately, their practical applications are hampered by unsatisfactory energy density. Because these superior properties of supercapacitors are princely based on the surface charge adsorption and desorption on carbon-based electrode materials of the electrical double-layer capacitors [8,9]. However, carbon-based materials usually suffer from low specific capacitance and low energy density due to their limited surface storage-energy mechanism [10]. As an alternative candidate, electrochemically active materials of iron oxides have attracted extensive attention to replacing carbon materials. Among them, hematite α-Fe_2O_3, as the most stable iron oxide, has become promising due to its abundance, high theoretical specific capacitance, low manufacturing cost, and low toxicity [11]. Especially, iron element owns various oxidation states, which can generate reversible redox reactions within the cathode voltage regions [12]. However, α-Fe_2O_3-based electrodes usually suffer from low electrical conductivity and structural stability resulting from their large crystal size and volume change during long-term charge/discharge processes, thereby leading to poor rate capability and low cycling stability [13–16]. Therefore, to improve the electrochemical performance of α-Fe_2O_3-based electrodes, two effective approaches have been explored including (1) reducing the particle size to the nanoscale, which can increase the effective surface area and shorten the diffusion paths of ions; (2) combining with conductive carbon materials such as graphene, carbon nanotubes (CNTs), and carbon nanofibers, which can enhance the electrochemical performance [17].

In this aspect, the most effective strategy is to directly fabricate nanosized α-Fe_2O_3 supported on carbon-based substrates, which can not only offer enough redox active sites but also fast ions/electrons transportation, thus providing enhanced rate capability and cycling performance. Although remark progresses have been achieved, it is still a big challenge to realize high mass-loading active materials. Also, the interfacial interaction between the nanosized α-Fe_2O_3 and the conductive substrate is rarely explored, which plays a crucial role in determining the rate capability and cycling stability of the electrode and the resultant device.

Herein, in this study we demonstrate a facile and cost-effective strategy to synthesize α-Fe_2O_3 nanoparticles decorated on

---

[*] Corresponding authors.
E-mail addresses: hzhang1@jxnu.edu.cn (H. Zhang), cmzhang@usts.edu.cn (C. Zhang), shaohua.jiang@njfu.edu.cn (S. Jiang).

https://doi.org/10.1016/j.cclet.2023.108283

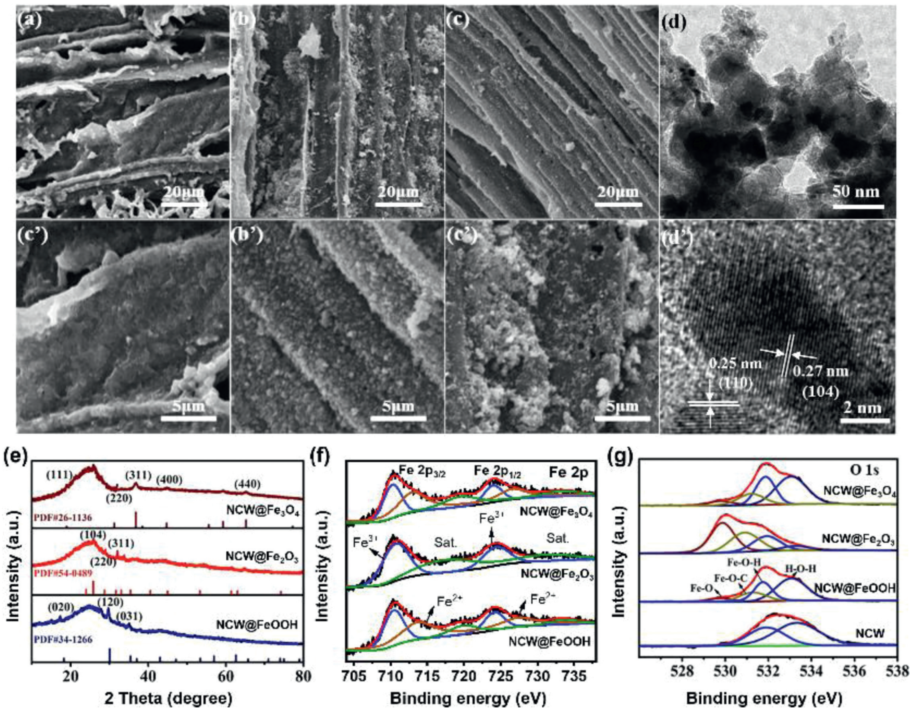

Fig. 1. Characterization of the obtained composites. SEM images of (a, a') the NCW@FeOOH synthesized at 100 °C, (b, b') the NCW@Fe_2O_3 synthesized at 300 °C, and (c, c') NCW@Fe_3O_4 synthesized at 500 °C. (d, d') TEM images of the NCW@Fe_2O_3 composite. (e) XRD patterns, (f) Fe 2p XPS spectra, and (g) O 1s XPS spectra of the obtained composites.

nitrogen-doped wood carbons (denoted as NCWs@Fe_2O_3) through a simple electrodeposition process, followed by post-heating treatment at low temperatures. We chose NCWs as the conductive matrix mainly because of their intrinsic three-dimensional porous structure originating from camellia oleifera branches, which is expected to provide sufficient space to support high mass-loading active materials [18–22]. At the same time, their surface oxygen-containing groups and defective sites function as the initial nucleation sites for the growth of iron oxide hydroxides. Subsequently, the post-heating treatment results in the formation of α-Fe_2O_3 nanoparticles, which can provide sufficient redox active sites on the NCW surface. The combination of conductive NCWs and α-Fe_2O_3 nanoparticles can facilitate the rapid electron transportation and the migration of electrolyte ions into the electroactive sites, which significantly enhances the electrochemical reaction kinetics. Furthermore, the formation of the interfacial Fe-O-C bonds not only enhances the electrically conductive contact but also further strengthens the binding energy between α-Fe_2O_3 nanoparticles and NCWs. As a result, the optimal NCW@Fe_2O_3 composite delivers extraordinary electrochemical performance including high specific capacitance, superior rate capability, as well as excellent long-term cycling stability.

As expected, iron oxide hydroxide synthesized at 100 °C was firmly anchored on NCWs surface (Figs. 1a and a'), which was proven to be transferred into iron oxides after post-heating treatment. Due to the existence of various structural forms of iron oxides, the effect of different sintering temperatures on the morphology and phase structure of iron oxides was first investigated. As shown in Figs. 1b and b', a uniform and smooth coating consisting of iron oxide nanoparticles was observed and closely attached to the NCW surface after being sintered at 300 °C. Further increasing the sintering temperature to 500 °C results in the remarkable aggregation of iron oxide nanoparticles (Figs. 1c and c'). X-ray diffraction (XRD) analysis indicates that the iron oxide hydroxide synthesized at 100 °C was in β-FeOOH configuration, which was then transferred to the hematite structure of the α-Fe_2O_3 phase at 300 °C and the spinel structure of the Fe_3O_4 phase at 500 °C (Fig. 1e) [23]. The products obtained at various temperatures were denoted as NCW@FeOOH, NCW@Fe_2O_3, and NCW@Fe_3O_4, respectively. High-resolution TEM image of NCW@Fe_2O_3 displays clear lattice fringes with a lattice spacing of 0.25 and 0.27 nm (Figs. 1d and d'), corresponding to the (110) and (104) crystal planes of α-Fe_2O_3, respectively [24]. Raman spectra of the NCW@Fe_2O_3 in Fig. S1 (Supporting information) NCW@Fe_2O_3 shows three characteristic peaks of the hematite structure at 226, 293 and 496 cm^{-1}, which can be assigned to the typical A_{1g} and E_g modes of Fe_2O_3, respectively, further confirming the formation of α-Fe_2O_3 phase [25].

X-ray photoelectron spectrometer (XPS) was further employed to characterize the surface composition and chemical bonding states of the NCW@Fe_2O_3 composite. As shown in Fig. S2a (Supporting information), the peaks of Fe 2p, C 1s, N 1s and O 1s are distinctly observed in all composites, which indicates that iron species were successfully anchored on the NCW surface. The C 1s spectra in Fig. S2b (Supporting information) display a strong C=C peak at 284.6 eV along with a low C-O shoulder at 286.2 eV and a small C=O tail at 288.9 eV, respectively, implying that conductive sp^2 carbon dominates the resultant composite [24]. Two characteristic peaks at 711.8 and 724.9 eV in the Fe 2p spectra are attributed to Fe $2p_{1/2}$ and Fe $2p_{3/2}$ spin-orbit coupling (Fig. 1f), respectively [26]. Notably, the presence of a satellite peak at 718.8 eV indicates the existence of Fe(III) species [27]. The O 1s spectra (Fig. 1g) of the NCW and iron oxide composites could be fitted to four subpeaks that are situated at 530.2, 531.4, 531.8 and 533.3 eV corresponding to Fe-O, C-O-Fe, Fe-O-H and O-C=C bond, respectively [28,29]. The existence of C-O-Fe demonstrates that the iron oxide species are linked with the NCW substrate by the C-O-Fe chemical bonding, which is beneficial for enhancing the interfacial contact between the active materials and the conductive matrix [30]. N_2 adsorption/desorption curve of the NCW@Fe_2O_3 composite in

Fig. S3 (Supporting information) presents a type I isotherm, indicating the presence of micro- and mesoporous structures. As a result, the NCW@Fe_2O_3 composite exhibits a lower specific surface area (642.3 m^2/g) than that of the NCW (981.8 m^2/g). These results demonstrate that a relatively high specific surface and abundant pore structure can be maintained after loading α-Fe_2O_3 nanoparticles on the NCW surface. Therefore, the hybridization of high surface area NCW and uniformly anchored α-Fe_2O_3 nanoparticles will significantly shorten the electron and ion diffusion paths and provide sufficient space for active sites to participate in the Faradaic redox reactions, thereby improving the electrochemical properties of the NCW@Fe_2O_3 composite.

It is worth noting that the mass-loading of α-Fe_2O_3 nanoparticles in the composite has an important effect on the voltage drop and the rate capability. Thus, the electrodeposition time is also a critical factor that should be considered. As a result, the NCW@Fe_2O_3 sample with an electrodeposition time of 10 min emerged as having the best electrochemical performance (Figs. S4 and S5 in Supporting information). The mass loading of α-Fe_2O_3 nanoparticles in the composite achieves as high as 24.3 wt% (Fig. S6 in Supporting information). The electrochemical properties of as-obtained composites were first investigated in a three-electrode cell (Fig. S7 in Supporting information). As expected, the NCW@Fe_2O_3 composite exhibits the best electrochemical performance. At a current density of 0.1 A/g, the NCW@Fe_2O_3 composite electrode possesses the highest specific capacitance of 603 F/g, which outperforms most of reported Fe_2O_3-based composite electrodes [31]. By contrast, the NCW@FeOOH and NCW@Fe_2O_3 electrodes exhibit low specific capacitances of 380 and 340 F/g, respectively.

To further investigate the electrochemical properties of the NCW@Fe_2O_3 composite electrode, cyclic voltammetry (CV) and galvanostatic charge-discharge (GCD) tests were carried out. As shown in Fig. 2a, CV curves of the NCW@Fe_2O_3 composite electrode at different scan rates ranging from 10 mV/s to 100 mV/s present a *quasi*-rectangular shape in a negative window from −1 V and 0 V *vs.* Hg/HgO, implying an ideal capacitive response. At the same time, no obvious shape change can be observed among the CV curves at different scan rates, indicating that the NCW@Fe_2O_3 electrode possesses good reversibility. Also, the GCD curves in Fig. 2b have no obvious voltage drop at various current densities, suggesting the low resistance and fast charge-discharge ability of the composite electrode. Besides, the specific capacitance of the NCW@Fe_2O_3 electrode is greatly higher than that of the NCW@FeOOH and NCW@Fe_3O_4 at each current density (Fig. 2c), which indicates the stable contribution of α-Fe_2O_3 nanoparticles in capacitance. Even at 50 A/g, the NCW@Fe_2O_3 electrode can deliver a specific capacitance of 405 F/g, corresponding to a capacitance retention of 67.2%. Furthermore, the NCW@Fe_2O_3 electrode also exhibits superior long-term cycling stability at 10 A/g. As shown in Fig. 2d, the specific capacitance of the NCW@Fe_2O_3 electrode still remained at 85.5% of the initial one after 10,000 cycles. The outstanding performance of the NCW@Fe_2O_3 electrode could be attributed to the synergistic effects of α-Fe_2O_3 nanoparticles and the conductive NCW matrix, which not only increases the number of active sites but also facilitates ion/electron transport during electrochemical reactions by decreasing the sluggish ion diffusion in the bulk phase of Fe_2O_3. Simultaneously, the formation of interfacial Fe-O-C bonding is responsible for excellent cycling stability, resulting in a more stable structure and little loss of capacitance during the charge-discharge processes. To confirm this, electrochemical impendence spectroscopy (EIS) of was carried out (Fig. S8 in Supporting information). In the low-frequency region, the NCW@Fe_2O_3 electrode shows a near-vertical line, showing ideal charge-transport efficiency. Simultaneously, the NCW@Fe_2O_3 also displays a lower charge transfer resistance than that of the NCW electrode, which indicates a faster electrochemical reaction on the electrode/electrolyte interface.

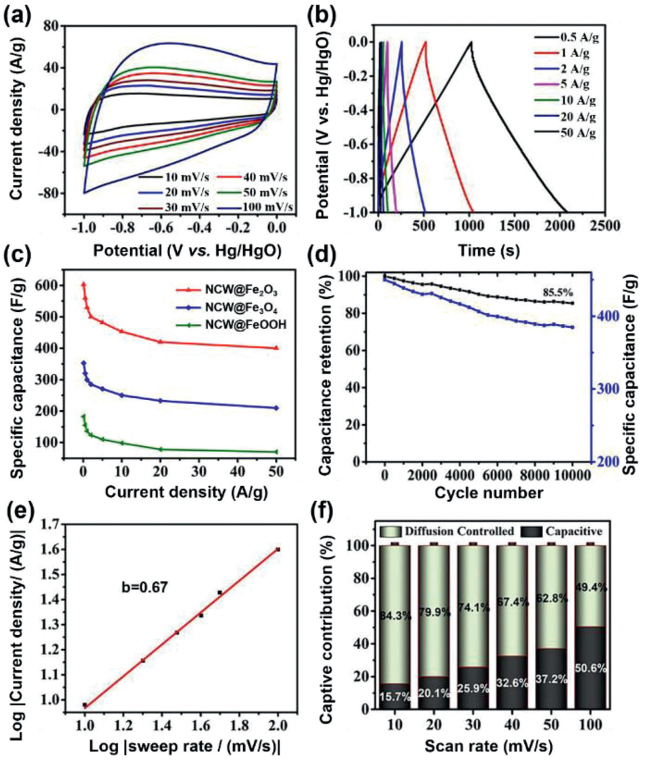

Fig. 2. Electrochemical performance of the NCW@Fe_2O_3 composite. (a) CV curves at various scan rates, (b) GCD curves at various current densities, (c) specific capacitance in various current densities, (d) cycling performance at 10 A/g, (e) functional relationship between current and scanning rate, and (f) capacity contribution at various scan rates.

To shed insight into the excellent electrochemical performance, the diffusion kinetics of the NCW@Fe_2O_3 electrode was further evaluated by analyzing the current response of CV curves at various scan rates. The peak current (i) and scan rate (v) have the following power-layer relationship [32]:

$$i = av^b \tag{1}$$

where both a and b are the adjustment constants. If the parameter b is close to 0.5, the diffusion-controlled process dominates in the electrochemical process; if b is close to 1.0, it will be the surface-redox-controlled process. The b value of the NCW@Fe_2O_3 electrode is calculated to be 0.67 (Fig. 2e), suggesting that the ionic-diffusion-controlled process contributes the major of the capacitance. As shown in Fig. 2f, the contribution from ionic diffusion reaches 84.3% at 10 mV/s, which can still achieve 49.4% at 100 mV/s.

To further evaluate the possibility of the practical application of the NCW@Fe_2O_3 electrode, an asymmetric supercapacitor (NCW//NCW@Fe_2O_3) was assembled by using the NCW as the anode and the NCW@Fe_2O_3 as the cathode. CV curves of the NCW//NCW@Fe_2O_3 device exhibits that with widening the electrochemical window, the polarization of the electrode arising from the evolution of oxygen becomes more and more obvious (Fig. 3a). Therefore, the maximum stable potential window of the asymmetric supercapacitor was chosen to be 1.0 V. At the same time, CV curves of the NCW//NCW@Fe_2O_3 device keep a similar rectangular shape at various scan rates (Fig. 3b). The GCD curves in Fig. 3c present a typical approximate symmetrical shape, suggesting that the device can deliver fast discharge at different current densities. Fig. 3d demonstrates that the NCW//NCW@Fe_2O_3 de-

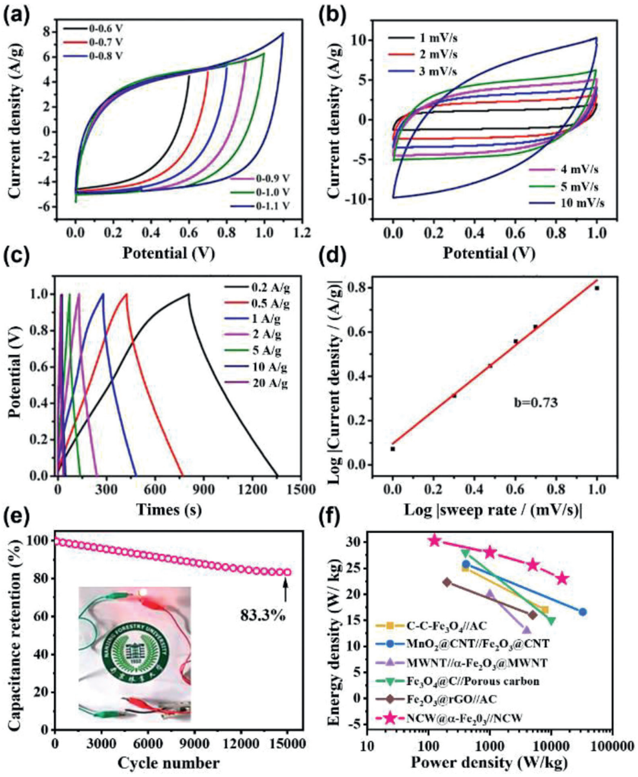

Fig. 3. Electrochemical properties of the NCW//NCW@Fe_2O_3 asymmetric supercapacitor. (a) CV curves under various voltage windows, (b) CV curves at various scan rates, (c) GCD curves at various current densities, (d) Functional relationship between current and scanning rate. (e) Cycling performance at 5 A/g, and (f) Ragone plots.

vice has an ionic diffusion-dominated capacity contribution. Cycling stability is of critical concern for asymmetric supercapacitors. As shown in Fig. 3e, the NCW//NCW@Fe_2O_3 device achieves a high capacitance retention of 83.3% after 15,000 cycles at 5 A/g, indicating outstanding long-term cycling stability. The Ragone plot of the NCW//NCW@Fe_2O_3 device (Fig. 3f) displays high energy and power densities in comparison with previously reported iron oxide-based supercapacitors [33–37]. Consequently, the asymmetric device achieves a maximum energy density of 30.3 Wh/kg at 125 W/kg, which is comparable to that of lead-acid batteries (30–50 Wh/kg). Moreover, the tandems of the symmetrical device can successfully light up a commercial LED (inset in Fig. 3e) after charging, demonstrating its promising potential for future practical applications.

In conclusion, we have fabricated the NCW@α-Fe_2O_3 composite as the electrode material for high-performance supercapacitors. The obtained α-Fe_2O_3 nanoparticles with a high mass-loading of 24.3 wt% are uniformly distributed on the NCW surface. The resultant NCW@Fe_2O_3 electrode exhibits excellent electrochemical performance including a high specific capacitance of 603 F/g at 0.1 A/g, superior rate capability, and high capacitance retention of 85.5% after 10,000 cycles at 10 A/g, which can be attributed to the synergistic effects of α-Fe_2O_3 nanoparticles and the NCW conductive matrix as well as the formation of interfacial Fe-O-C bonds. Moreover, the corresponding asymmetrical device displays outstanding cycling stability and delivers a high energy density of 30.3 Wh/kg at 125 W/kg. This work paves a new way to develop low-cost and high-mass-loading iron oxide composites as high-performance electrode materials for supercapacitors.

Declaration of competing interest

The authors declare that they have no known competing financial interests or personal relationships that could have appeared to influence the work reported in this paper.

Acknowledgment

The work was supported by the Natural Science Foundation of Jiangxi Province of China (No. 20224BAB214008).

Supplementary materials

Supplementary material associated with this article can be found, in the online version, at doi:10.1016/j.cclet.2023.108283.

References

[1] Y. Wang, L. Zhang, H. Hou, et al., J. Mater. Sci. 56 (2021) 173–200.
[2] Y. Bai, C. Liu, T. Chen, et al., Angew. Chem. Int. Ed. 60 (2021) 25318–25322.
[3] J. Gu, Y. Peng, T. Zhou, et al., Nano Res. Energy 1 (2022) 9120009.
[4] S. Zheng, Q. Li, H. Xue, H. Pang, Q. Xu, Natl. Sci. Rev. 7 (2019) 305–314.
[5] F. Wang, L. Chen, H. Li, et al., Chin. Chem. Lett. 31 (2020) 1986–1990.
[6] J. Xiao, H. Li, H. Zhang, et al., J. Bioresour. Bioprod. 7 (2022) 245–269.
[7] S.I. Wong, H. Lin, T. Ma, et al., Mater. Rep. Energy 2 (2022) 100093.
[8] M.D. Stoller, S. Park, Y. Zhu, J. An, R.S. Ruoff, Nano Lett. 8 (2008) 3498–3502.
[9] X. Xu, L. Yang, W. Zheng, et al., Mater. Rep. Energy 2 (2022) 100080.
[10] W. Lv, Z. Li, Y. Deng, Q.H. Yang, F. Kang, Energy Storage Mater. 2 (2016) 107–138.
[11] Y. Hu, C. Guan, Q. Ke, et al., Chem. Mater. 28 (2016) 7296–7303.
[12] X. Lu, Y. Zeng, M. Yu, et al., Adv. Mater. 26 (2014) 3148–3155.
[13] X.F. Lu, X.Y. Chen, W. Zhou, Y.X. Tong, G.R. Li, ACS Appl. Mater. Interfaces 7 (2015) 14843–14850.
[14] Z. Ji, L. Chen, H. Yu, et al., Chem. Eng. J. 450 (2022) 137942.
[15] Y. Wang, Z. Du, J. Xiao, W. Cen, S. Yuan, Electrochim. Acta 386 (2021) 138486.
[16] J. Jiang, J. Liu, Interdiscip Mater. 1 (2022) 116–139.
[17] Z. Wang, C.J. Liu, Nano Energy 11 (2015) 277–293.
[18] Y. Qin, Y. Liao, J. Liu, et al., J. For. Eng. 6 (2021) 1–13.
[19] L. Chen, X. Wei, F. Wang, et al., Chin. Chem. Lett. 33 (2022) 2635–2638.
[20] Y. Chen, Q. Zhang, M. Chi, et al., J. For. Eng. 7 (2022) 127–135.
[21] L. Ding, X. Han, L. Chen, S. Jiang, J. Bioresour. Bioprod. 7 (2022) 295–305.
[22] B. Yin, W. Du, Y. Zhang, et al., J. For. Eng. 7 (2022) 38–45.
[23] Y. Zhu, S. Cheng, W. Zhou, et al., ACS Sustain. Chem. Eng. 5 (2017) 5067–5074.
[24] H. Zhang, C. Lu, C. Chen, et al., ChemElectroChem 4 (2017) 1990–1996.
[25] H. Mansour, H. Letifi, R. Bargougui, et al., Appl. Phys. A 123 (2017) 787.
[26] P. Zhao, W. Li, G. Wang, et al., J. Alloy. Compd. 604 (2014) 87–93.
[27] C.J. Jia, L.D. Sun, F. Luo, et al., J. Am. Chem. Soc. 130 (2008) 16968–16977.
[28] X. Zhang, Z. Yao, Y. Zhou, et al., Chem. Eng. J. 411 (2021) 128535.
[29] B. Li, H. Pang, H. Xue, Chin. Chem. Lett. 32 (2021) 885–889.
[30] H. Liu, J. Zhu, Z. Li, et al., Chem. Eng. J. 403 (2021) 126325.
[31] X. Cheng, X. Gui, Z. Lin, et al., J. Mater. Chem. A 3 (2015) 20927–20934.
[32] F. Wan, L. Zhang, X. Dai, X. Wang, Z. Niu, J. Chen, Nat. Commun. 9 (2018) 1656.
[33] X. Zhao, C. Johnston, P.S. Grant, J. Mater. Chem. 19 (2009) 8755–8760.
[34] T. Gu, B. Wei, J. Mater. Chem. A 4 (2016) 12289–12295.
[35] X. Li, L. Zhang, G. He, Carbon 99 (2016) 514–522.
[36] H. Fan, R. Niu, J. Duan, W. Liu, W. Shen, ACS Appl. Mater. Interfaces 8 (2016) 19475–19483.
[37] Y. Wang, H. Li, W. Yang, et al., Diam. Relat. Mater. 130 (2022) 109526.